

THE ROLE OF GALACTIC COLD GAS IN LOW-LEVEL SUPERMASSIVE BLACK HOLE ACTIVITY

ERIK D. ALFVIN¹, BRENDAN P. MILLER², MARTHA P. HAYNES³, ELENA GALLO⁴, RICCARDO GIOVANELLI³,
REBECCA A. KOOPMANN⁵, EDMUND HODGES-KLUCK⁴, JOHN M. CANNON¹

Draft version November 5, 2018

Abstract

The nature of the relationship between low-level supermassive black hole (SMBH) activity and galactic cold gas, if any, is currently unclear. Here, we test whether central black holes may feed at higher rates in gas-rich galaxies, probing SMBH activity well below the active regime down to Eddington ratios of $\sim 10^{-7}$. We use a combination of radio data from the ALFALFA survey and from the literature, along with archival X-ray flux measurements from the *Chandra* X-ray observatory, to investigate this potential relationship. We construct a sample of 129 late-type galaxies, with $M_B < -18$ out to 50 Mpc, that have both HI masses and sensitive X-ray coverage. Of these, 75 host a nuclear X-ray source, a 58% detection fraction. There is a highly significant correlation between nuclear X-ray luminosity L_X and galaxy stellar mass M_{star} with a slope of 1.7 ± 0.3 , and a tentative correlation (significant at the 2.8σ level) between L_X and HI gas mass M_{HI} . However, a joint fit to L_X as a function of both M_{star} and M_{HI} finds no significant dependence on M_{HI} (slope 0.1 ± 0.3), and similarly the residuals of $L_X - L_X(M_{\text{star}})$ show no trend with M_{HI} ; the apparent correlation between L_X and M_{HI} seems to be entirely driven by M_{star} . We demonstrate quantitatively that these results are robust against X-ray binary contamination. We conclude that the galaxy-wide cold gas content in these spirals does not strongly correlate with their low-level supermassive black hole activity, and suggest fueling is a localized process.

Subject headings: galaxies – black holes; accretion; cold gas

1. INTRODUCTION

Nearly every moderately massive galaxy (i.e., $M_{\text{star}} > 10^{10} M_{\odot}$) appears to contain a supermassive black hole (SMBH) at its center, with M_{BH} correlating with the bulge stellar velocity dispersion σ , optical luminosity, or stellar mass (e.g., Gültekin et al. 2009; McConnell & Ma 2013, and references therein). Some active galactic nuclei are rapidly accreting gas at near Eddington rates, but most SMBHs in the local universe are weakly accreting or quasi-quiescent, like our own Milky Way. The galactic processes that drive SMBH accretion are complex and gas movement within disks is not yet well understood. However, black hole mass, which necessarily increases through accretion, is well studied across different types of galaxies. Compared to bulge-dominated early-type galaxies, where the bulge accounts for nearly all of the luminosity and stellar mass, late-type galaxies follow a $M_{\text{BH}} - \sigma$ relation with a similar slope (black hole mass positively correlating with higher velocity dispersion) but a lower intercept. The SMBHs hosted in spirals are therefore on average less massive by a factor of ~ 2 than in ellipticals at a given σ (McConnell & Ma 2013), although some studies do find spirals and ellipticals show consistent trends (Graham & Scott (2013)). Late-type galaxies also offer some disk tracers of SMBH mass, such as

spiral arm pitch angle (e.g., Davis et al. 2014, and references therein), and it is now clear that there are bulgeless galaxies with SMBHs (Reines et al. 2011; Simmons et al. 2013; Bizzocchi et al. 2014; Satyapal et al. 2014). SMBH masses do not appear to correlate with disk or pseudobulge absolute magnitudes (Kormendy et al. 2011), although see also discussion in Läscher et al. (2014). These factors suggest that black hole growth could be tied to galactic gas, and not only to bulge properties. The rate of major mergers is lower for late-type galaxies than for early-type galaxies (spiral morphology can be destroyed in major mergers, although gas rich mergers may preserve or regrow disks; Hopkins et al. 2009), so they are less able to activate and significantly grow their SMBHs through mergers.

The relationship between SMBH growth and activity, and host galaxy evolution is complex (Shankar et al. 2009). Cold gas reservoirs could fuel star formation and SMBH accretion (the latter perhaps indirectly, from stellar winds) and we would observe a positive correlation between SMBH accretion rate and cold gas mass. On the other hand, if SMBH accretion feedback heats and expels gas and thereby shuts down star formation, we might observe a negative correlation. Or, particularly in smaller galaxies with smaller SMBHs, timescale mismatches and a limited energy budget may causally decouple these processes (e.g., Kormendy & Ho 2013, and references therein). Here, we explore the black hole accretion - cold gas mass relationship through investigating how nuclear X-ray luminosities are linked to total HI masses. This work both complements and extends previous studies in that we investigate all detectable SMBH activity in nearby, late-type galaxies rather than only known active galactic nuclei (AGNs); indeed, the majority of galaxies in our sample do not have optical indica-

¹ Department of Physics and Astronomy, Macalester College, Saint Paul, MN 55105, USA

² Department of Chemistry and Physical Sciences, The College of St. Scholastica, Duluth, MN 55811, USA

³ Center for Radiophysics and Space Research, Space Sciences Building, Cornell University, Ithaca, NY 14853, USA

⁴ Department of Astronomy, University of Michigan, Ann Arbor, MI 48109, USA

⁵ Department of Physics and Astronomy, Union College, Schenectady, NY 12308, USA

tors of nuclear activity.

As also noted for nearby early-type galaxies, there is more than sufficient (hot) gas near the central regions (Soria et al. 2006) to produce observed levels of activity. That being said, it seems plausible that additional (cold) gas, either directly available for SMBH accretion or indirectly involved via star formation that then adds mass loss from winds, would increase the accretion rate and consequent X-ray emission. We might expect that galaxies with larger total HI masses transport more of that cold gas to the central region, and have more active SMBHs. The expected rates of mass accretion for these late-type galaxies correspond to doubling times of tens of Gyr, but addressing this question is nonetheless important for understanding SMBH growth. A positive correlation between galaxy-wide HI mass and nuclear X-ray emission might suggest that cold gas is important for activity also in powerful AGNs. In this context SMBH growth would not need to be self-regulated by feedback but rather would depend on the transport properties (e.g., torque-limited accretion; Angles-Alcazar et al. 2013).

Our HI masses are primarily drawn from the ALFALA survey. ALFALA is a blind HI survey using the Arecibo L-band Feed Array (ALFA) at the Arecibo telescope to scan a portion of the $0^\circ < \delta < 36^\circ$ sky at frequencies surrounding the HI 1420 MHz line (1335–1435 MHz). The $\alpha 40$ preliminary catalog (40% coverage complete) is presented in Haynes et al. (2011). Here, we use the new $\alpha 70$ catalog⁶ (Haynes et al., in preparation; results for 70% coverage) to obtain HI masses for a sample of local spiral galaxies. We supplement the ALFALA data with literature HI masses taken from the HyperLeda database⁷ (Makarov et al. 2014)

For X-ray luminosities we use archival *Chandra* data. High angular resolution *Chandra* X-ray observations provide a proven method of identifying low-level supermassive black hole activity in early-type galaxies (e.g., Zhang et al. 2009; Gallo et al. 2010; Pellegrini 2010; Miller et al. 2012). In contrast to ellipticals, which do not typically contain large amounts of cold gas (particularly in clusters; e.g., Grossi et al. 2009 and references therein), spirals are often gas-rich. A gas-rich environment provides a complicating contamination possibility from high-mass X-ray binaries (which can be present near sites of recent star formation), but here too *Chandra* generally has sufficient resolution to identify SMBH activity (e.g., Mathur et al. 2010; O’Sullivan et al. 2014; Tzanavaris et al. 2014). We develop a statistical technique to quantify potential X-ray binary contamination and account for it in our linear regression modeling. The X-ray coverage provides sensitivities pushing down to luminosities relative to Eddington of $\sim 10^{-7}$, well below the formally active AGN regime.

This paper is organized as follows. Section 2 describes the sample selection and calculation of HI masses and X-ray luminosities. Section 3 presents correlation analyses, controlling for potential X-ray binary contamination, measurement uncertainties, and X-ray upper limits. Section 4 discusses additional multiwavelength activity indicators and the relationship between star formation rates,

⁶ <http://egg.astro.cornell.edu/alfalfa/data/>

⁷ <http://leda.univ-lyon1.fr/>

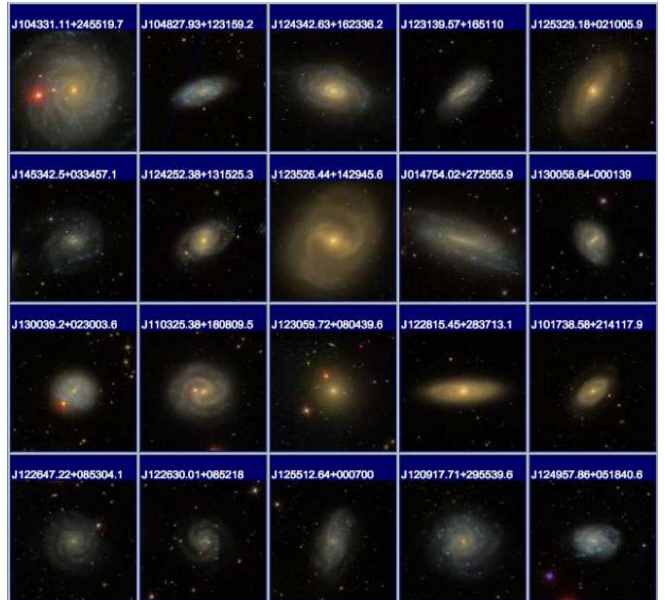


Figure 1. SDSS optical cutouts of 20 representative galaxies in our sample with ALFALFA HI measurements. All show clear spiral morphology.

cold gas, and SMBH activity, and potential future work.

2. SAMPLE SELECTION AND CHARACTERISTICS

Here we describe the optical selection, measurement of HI masses, and determination of X-ray coverage for our sample. SDSS cutouts verifying spiral morphology for 20 representative galaxies with ALFALFA HI measurements are provided in Figure 1. X-ray, optical, and ALFALFA HI data are shown for reference for NGC 4501, one of the most luminous spirals in our sample, in Figure 2.

2.1. Optical selection of parent sample

We selected a volume-limited parent sample of late-type galaxies from the HyperLeda database. We required each source to be a spiral galaxy with morphological type between $t = 1$ (Sa) and $t = 7$ (Sd) – note that this excludes S0 galaxies – and imposed a luminosity limit of $M_B < -18$. We additionally restrict consideration to spirals with inclination between the polar axis and the line-of-sight $< 70^\circ$ (i.e., not edge-on) to reduce the complicating effects of internal extinction. We initially consider all late-type galaxies with a distance modulus less than 34.8 (i.e., within $\simeq 90$ Mpc).

The HyperLeda SQL query that we used to construct our parent sample is: `select objname, al2000, de2000, t, modz, mabs, bvtc, m21c where modz <= 34.8 and mabs <= -18 and t >= 1 and t <= 7 and incl < 70 order by mabs`

There are 6491 galaxies that meet these criteria. Distances in Mpc for the full parent sample are initially calculated from the redshift distance modulus given in HyperLeda. After cross-matching to ALFALFA and *Chandra* coverage and further refining selection criteria (see below), for the final sample of 129 spirals with HI masses and X-ray coverage we update the distances (and all associated luminosities, absolute magnitudes, and masses) for the 126/132 galaxies that have non-redshift measure-

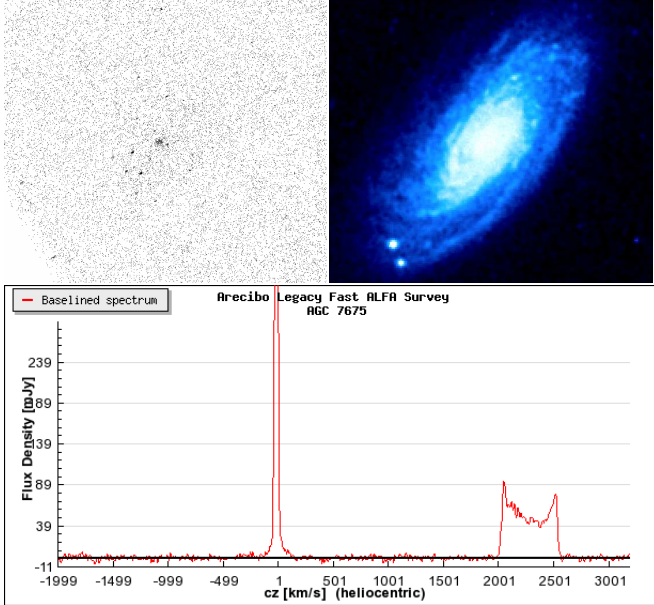


Figure 2. Left: Full band X-ray *Chandra* image of NGC 4501, showing nuclear X-ray source as well as a few XRBs. Right: DSS optical image at matched angular scale. Bottom: ALFALFA HI spectrum, showing double-peaked emission at the redshift of NGC 4501. The narrow emission line at $cz \sim 0$ is due to the Milky Way.

ments available in the Extragalactic Distance Database⁸ (EDD; Tully et al. 2009) listing of preferred distances, which is restricted to $v < 3000$ km s⁻¹.

For the galaxies in the parent sample, we calculate the stellar mass in solar units using the relations given in Bell et al. (2003) as

$$M_{\text{star}} = 1.737(B - V) - 0.942 + 0.4(B_{\odot} - B)$$

Here the absolute magnitude for the sun is taken to be $B_{\odot} = 5.515$.⁹ The $B - V$ color is the difference between the B and V optical magnitudes corrected for galactic extinction. For the parent sample, M_{star} is not calculated for galaxies that lack $B - V$ colors in HyperLeda; for the final sample of 129 spirals, missing $B - V$ colors (24% of entries) are set to the median 0.56 value.

We calculate the star formation rate (SFR) for the final sample of 129 spirals by cross-matching to the All-Sky GALEX UV catalog¹⁰. A match radius of 6'' produces 46 galaxies with both FUV and NUV magnitudes. UV fluxes trace star formation rate because they include contributions from high-mass short-lived hot stars, and UV-derived SFRs are not systematically offset from H α estimates (Bell & Kennicutt 2001).¹¹ We use equations 6, 7, and 8 from Salim et al. (2007). The FUV magnitude is corrected for internal extinction using the FUV-NUV color as

$$FUV_{\text{corr}} = FUV - 2.99 \times (FUV - NUV) - 0.27$$

and also corrected for a typical Milky Way reddening of 0.2 magnitudes.¹² After converting corrected FUV magnitudes to flux densities and then luminosity densities (in units of erg s⁻¹ Hz⁻¹), the SFR in units of M_{\odot} yr⁻¹, is calculated as

$$\log SFR = \log L_{\text{FUV,corr}} - 28.165$$

A similar recipe for calculating SFRs is given by Lee et al. (2011; see also Karachentsev & Kaisina 2013) as $\log SFR = 2.78 - 0.4f_{\text{uv}} + 2 \log d$ with f_{uv} the extinction-corrected FUV magnitude and d the distance in Mpc. The All-Sky GALEX UV catalog magnitudes are slightly fainter than the elliptical aperture photometry done by Lee et al. (2011); this is corrected by increasing our SFRs by 0.03 dex, which is the mean difference for overlapping galaxies at $d < 10$ Mpc.

We verified that the late-type classifications from HyperLeda were correct through inspection of SDSS cutouts (Figure 1).

2.2. HI masses

The ALFALFA survey has a limiting two-pass sensitivity of 1.8 mJy per beam and a half power beam width of 3.3'x3.8' for each of seven feeds (Giovanelli et al. 2005). Nearly all ALFALFA HI detected galaxies have an optical counterpart (Haynes et al. 2011). The ALFALFA catalog uses source codes to classify objects. Code 1 objects have a high signal-to-noise ratio ($S/N > 6.5$) and are high confidence detections. Objects with a source code of 2 have a moderate signal-to-noise ratio ($4 < S/N < 6.5$) with an optical counterpart at the same redshift, while entries with a source code of 3 also have a moderate signal-to-noise ratio but without an optical counterpart; deeper follow-up radio observations indicate that code 2 objects are generally reliable while code 3 events are generally spurious. Code 4 and 5 objects have lower signal to noise ratios or RFI contamination and are not reliable sources. Finally, code 9 objects are likely high velocity clouds within the Milky Way. We used ALFALFA sources with code 1 and 2 only.

To get HI data, we matched the resulting HyperLeda source positions to those in $\alpha 70$ with a search radius of 1 arc-min. Even with the ALFALFA beam size (~ 50 projected kpc for a source at 50 Mpc) source confusion is minimal, and the mass of the spiral dominates over any small satellite galaxies. We retrieved HI fluxes from both $\alpha 70$ and HyperLeda literature when possible. We examined all galaxies labeled as multiple in HyperLeda, and crudely categorized their degree of interaction on a scale from 0–3, where 3 indicates merging. (We also eliminated NGC 3314A at this stage because it is superimposed on another galaxy.) Of the 129 galaxies in the final sample, only NGC 3256 and NGC 7727 seem to be in the process

⁸ <http://edd.ifa.hawaii.edu/>

⁹ <http://sites.google.com/site/mamajeksstarnotes/basic-astronomical-data-for-the-sun>

¹⁰ http://archive.stsci.edu/prepds/gcat/gcat_casjobs.html

¹¹ While FUV and H α derived SFRs agree when internal extinction is taken into account for normal spirals such as considered here, this is not necessarily the case for dwarfs (Lee et al. 2009; McQuinn et al. 2015).

¹² While the SFRs are not strongly dependent on the sightline through the Milky Way, for a check of seven random galaxies the median, minimum, maximum, and standard deviation Galactic reddening is 0.24, 0.10, 0.44, and 0.12. These are calculated from Landolt A_V given in NED, taking $R_V = 3.1$ to find $E(B - V)$, then using the Fitzpatrick (1999) parameterization, implemented in IDL as `fm.unred`, at the FUV effective wavelength of 1516Å.

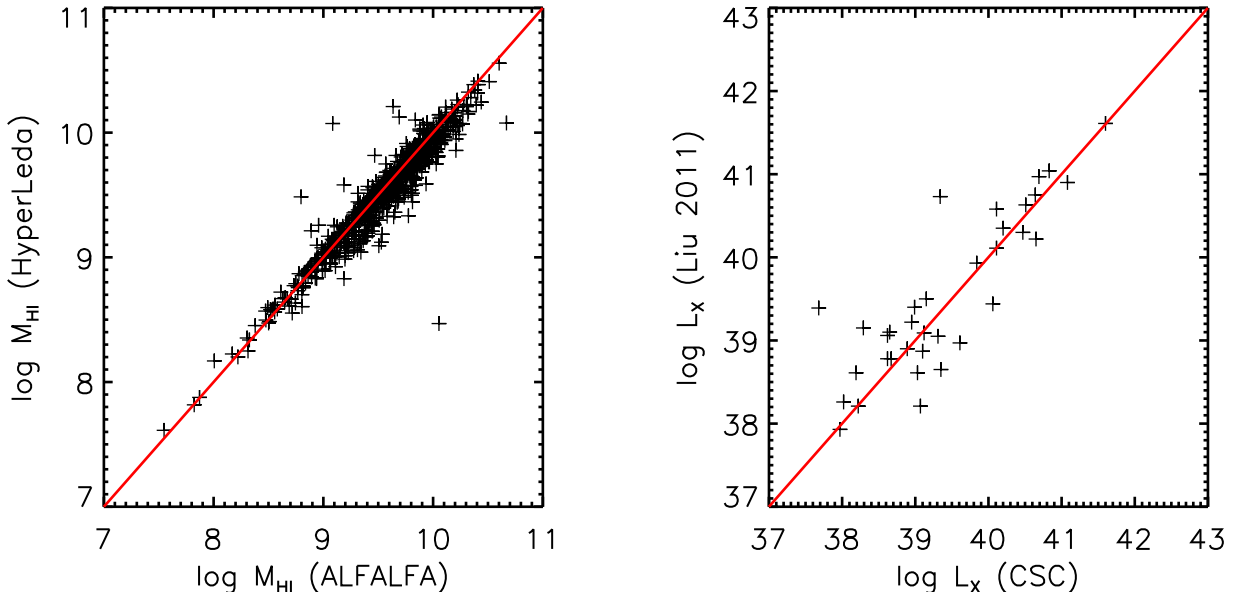


Figure 3. Left: HI masses from HyperLeda against new ALFALFA HI measurements. Right: X-ray luminosity from Liu (2011) against values from the Chandra Source Catalog. The red line indicates equal measurement values.

of merging. There are an additional 17 galaxies that are multiple, of which 5 (NGC2993, NGC3395, NGC5194, NGC5427, and NGC5954) show clear interaction signatures such as tidal tails.

The HI mass was calculated from the relationship

$$M_{\text{HI}} = 2.36 \times 10^5 d_{\text{Mpc}}^2 S_{\text{HI}}$$

and is expressed as a logarithm. From the parent sample there are 3966 spirals that have either ALFALFA or HyperLeda literature HI measurements. In Figure 3 (left panel), we plot HI masses derived from each catalog for 780 sources with data in both. For this comparison for all sources we used redshift distances from HyperLeda. The agreement between catalogs is excellent; the difference has median, mean, and standard deviation of 0.003, -0.008 , and 0.158 dex. A few of the individual literature measurements in HyperLeda may have been taken at higher angular resolution than the ALFALFA survey, and resolve out flux; we prioritize ALFALFA data.

2.3. X-ray luminosities and limits

For X-ray coverage, *Chandra* is the optimal observatory with which to determine nuclear X-ray luminosities for our sample of local late-type galaxies due to its high angular resolution, which helps avoid contamination from X-ray binaries that may be present throughout the galaxy including near the (projected) center. Archival observations from *ROSAT* or *XMM-Newton* do not provide sufficient angular resolution and consequently are not considered. An inherent limitation of this dataset is that most of the galaxies with *Chandra* coverage were targeted rather than serendipitous and we cannot control for the original motivation for targeting these particular galaxies, or for the inhomogeneous sensitivities.

The *Chandra* Source Catalog (CSC; Evans et al. 2010) is a list of X-ray detected point sources from archived

Chandra observations. The CSC contains many parameters including X-ray fluxes for each source. Where an X-ray source is not present at the specified coordinates, the catalog provides upper limit sensitivities, which we include in our analysis. The CSC includes imaging spectroscopy (ACIS-I or ACIS-S without gratings) data that is public as of 2011.

The HyperLeda source positions were matched to CSC X-ray sources with a search radius of 2 arc-seconds to obtain only nuclear matches. The X-ray luminosities were calculated from CSC full-band source fluxes using HyperLeda distance moduli for each source as simply $L_X = 4\pi d^2 f_X$ (i.e., no k -correction is required for these low-redshift objects) and are also expressed as logarithms. For sources that had *Chandra* coverage but were not detected in the CSC, we retrieved the sensitivities at those positions. The sensitivities were then used as upper limits in the fitting.

We also obtained nuclear X-ray luminosities from the catalog compiled by Liu (2011). The agreement between the CSC and Liu luminosities is also generally good (Figure 3, right), with offset median/mean/standard deviation for 35 objects of $-0.11/-0.10/0.52$.

For completeness, we also confirmed the X-ray flux measurements for a random set of 15 sources with archival *Chandra* data. After reducing the observations using the Chandra Interactive Analysis of Observations (CIAO) software, we identified the central X-ray source and extracted the flux from a circular aperture, then subtracted the background. As expected, our hand-measured fluxes closely matched those given in the catalog search.

Our initial optical selection of the parent sample went out to a distance of 90 Mpc. We examined the detection fraction of X-ray nuclear sources as a function of distance (Figure 4, left) to see how deep we could reasonably make our final sample. A detection refers to a

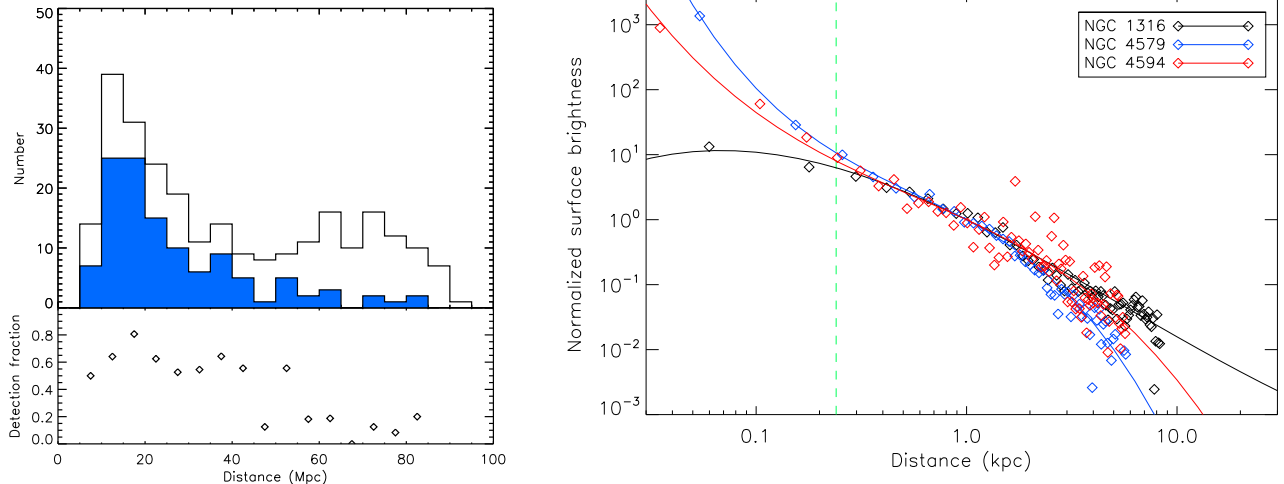


Figure 4. *Left:* Histogram of *Chandra* X-ray coverage (open) and nuclear X-ray source detection (filled) as a function of distance. We impose a cut of $d < 50$ Mpc to maintain a high detection fraction. *Right:* X-ray surface brightness profiles for three example galaxies. NGC 1316 (Fornax A) is a complex quasi-lenticular with radio jets and a weak nuclear X-ray source, excluded from our sample. NGC 4579 is an Sb and NGC 4594 is an Sa spiral; both are also Seyfert 2 galaxies and contain a nuclear X-ray source powered by low-level supermassive black hole activity. The vertical line shows $1''$ at 50 Mpc.

spiral in this HyperLeda sample that also has a *Chandra* CSC source within $2''$ of the optical position. It is apparent that there is a significant decline in the detection fraction beyond 50 Mpc. We also examined X-ray surface brightness profiles from a few deep *Chandra* observations of relatively nearby galaxies (Figure 4, right) to map typical distributions of X-ray binaries (and hot gas) as a function of radial distance. These profiles suggested that it is possible to identify nuclear sources above the radial X-ray binary contamination out to about 50 Mpc. (This does not guarantee that a central source is associated with the SMBH, but the likelihood increases with $L_X > 40$, which many of our galaxies surpass; see Section 3.2) We therefore imposed $d < 50$ Mpc for further analysis of X-ray properties.

We rechecked the luminosity cut with the updated EDD distances, and discarded UGC 05707, NGC 5474, and NGC 5585 as they no longer satisfy $M_B < -18$. After examining Digitized Sky Survey images, we additionally discarded NGC 4594, NGC 0672, and PGC 052935 as having likely incorrect inclinations in HyperLeda (i.e., they are too edge-on for our purposes). The resulting optical sample contains spiral galaxies with B-band optical magnitudes < -18 within 50 Mpc that are not edge-on.

Our final sample of spirals with *Chandra* coverage and HI data then consists of 129 galaxies, of which 75 (58%) have a central source detected in X-rays. Table 1 lists the optical properties, HI mass, and nuclear X-ray luminosity or limit for each galaxy.

3. CORRELATION ANALYSIS

We illustrate the relationship between stellar mass and cold gas fraction (of the baryonic mass), here calculated as $M_{\text{HI}}/(M_{\text{HI}} + M_{\text{star}})$, in Figure 5. We perform linear regression using the IDL routine `robust_linefit.pro`, which uses iterative bisquare weighting. The best-fit slope, calculated robustly against outliers, is -0.50 ± 0.02 . Our data therefore show the expected trend that optically brighter and more massive spirals possess more HI

gas in absolute terms (because the slope is > -1) but have lower gas fractions (because the slope is < 0). The correlation is extremely significant with $p < 0.001$. This trend has been quantified using $\alpha 40$ ALFALFA data by Huang et al. (2012, 2014; see also Maddox et al. 2015) and we here illustrate it with the new $\alpha 70$ catalog for nearby spirals. The slope of $\simeq -0.50$ that we find for these galaxies is consistent with the slope of -0.57 for $M_{\text{gas}}/M_{\text{star}}$ found by Peebles & Shankar (2011); our slope is slightly shallower because we examine gas mass in relation to baryonic mass rather than only stellar mass.

There appear to be some outliers at low gas fractions in Figure 5. We investigated the nature of galaxies that lie 2σ above or below the mean. Three galaxies are classified as outliers: NGC 4448 is red, likely a star-forming spiral, NGC 4450 is a cluster galaxy in Virgo but otherwise normal, and NGC 7727 is a late-stage merger with tails. Each of these characteristics could be responsible for lowering the galaxies' gas fractions. It is interesting that there are no outliers with high gas fractions, while lower than average gas fractions are common for any given M_{star} . It appears that gas is easier to use than to store in spiral galaxies.

We also investigated the relationship between M_{HI} and M_B . First we fit M_{HI} versus M_B , then we fit M_B versus M_{HI} . Here we calculated the best-fit trend using the bisector slope since it is not clear which direction the causal relationship, if any, should go (Isobe et al. 1990). We find a strong correlation, but this is not surprising since M_B is used to calculate M_{star} , so this is another perspective on the gas fraction trend noted above.

3.1. X-ray fitting

We investigate nuclear X-ray luminosity versus stellar mass and HI mass. We use the Bayesian linear regression code of Kelly (2007), implemented in IDL as `linmix_err.pro`, to determine the correlation slope and intercept taking both measurement uncertainties and the X-ray upper limits into account. We report the preferred

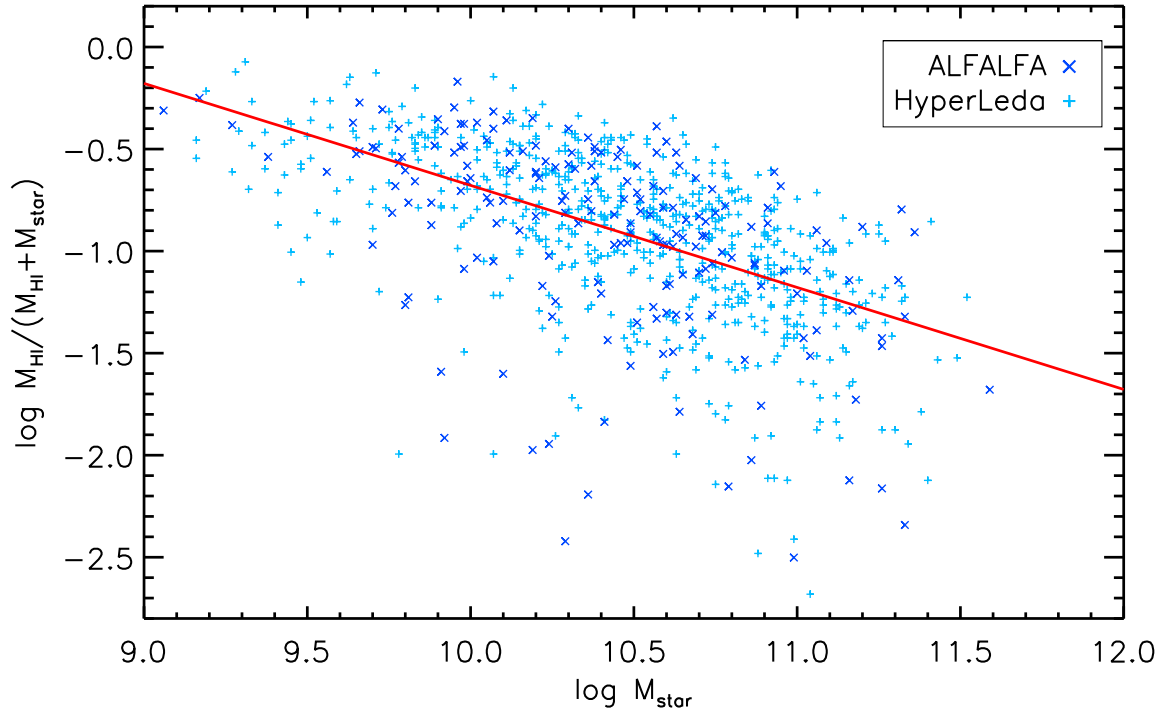


Figure 5. Comparison of HI to stellar mass, with fractional $M_{\text{HI}}/(M_{\text{HI}} + M_{\text{star}})$ as a function of M_{star} . There is a decline in the gas fraction of late-type galaxies with increasing stellar mass (e.g., Huang et al. 2012; Maddox et al. 2015). The solid red line shows the robust best-fit linear regression model.

model parameters as the median of 10000 draws from the posterior distribution, with uncertainties corresponding to 1σ from the 16th and 84th percentiles.

For the stellar mass versus nuclear X-ray luminosity, fit as

$$\log L_X - 39 = \alpha + \beta \times (\log M_{\text{star}} - 10.5)$$

the best-fit intercept, slope, and intrinsic scatter are $\alpha = 0.18 \pm 0.13$, $\beta = 1.73 \pm 0.26$, and $\sigma_0 = 1.09 \pm 0.11$. While the intrinsic scatter is large, there is a highly significant correlation between the variables, in the sense that optically-brighter and more massive spiral galaxies also have greater L_X values. The slope of $\beta = 1.73 \pm 0.26$ is consistent with $L_X \propto M_{\text{star}}^2$, which might be expected for Bondi accretion where $\dot{m} \propto m^2$, if the local mass m were to scale with the total stellar mass M_{star} , and further presuming that the black hole mass M_{BH} were a fixed fraction of M_{star} and that L_X scales with \dot{m} . A slope of $\beta \sim 1$, corresponding to a uniform Eddington ratio under these assumptions, seems ruled out for our spirals. Since these assumptions may not hold – in particular, the local gas supply may not be closely linked to the overall galaxy gas content – we refrain from drawing particular conclusions from the best-fit slope.

For the HI mass versus nuclear X-ray luminosity, fit as

$$\log L_X - 39 = \alpha + \beta \times (\log M_{\text{HI}} - 9.5)$$

the best-fit intercept, slope, and intrinsic scatter are $\alpha = -0.16 \pm 0.15$, $\beta = 0.90 \pm 0.32$, and $\sigma_0 = 1.33 \pm 0.13$.

The intrinsic scatter is quite large, but there is tentative evidence for a positive correlation between HI mass and nuclear X-ray luminosity; the slope is greater than zero at the $\sim 2.8\sigma$ level. These correlations are shown in Figure 6 (top panels) with the best-fit linear relations considering all sources (solid lines). For completeness, we also show the regression results for the galaxies with nuclear X-ray detections only (dashed lines). *Chandra* detections and upper limits are indicated with plus symbols and arrows, respectively.

However, we then fit L_X as a function of both M_{star} and M_{HI} and found that the dependence upon M_{HI} in this joint fit has a slope of 0.14 ± 0.29 , consistent with zero. The dependence upon M_{star} in the joint fit has a slope of 1.69 ± 0.30 . Further, the residuals of $L_X - L_X(M_{\text{star}})$ show no trend with M_{HI} . This contrasts with the residuals for $L_X - L_X(M_{\text{HI}})$ which still do show a trend with M_{star} (Figure 6, bottom panels). The tentative relationship between L_X and M_{HI} appears to be entirely driven by M_{star} .

As a check, we also fit L_X as a function of both M_{star} and M_{HI} restricted to the 124 galaxies with distances less than 40 Mpc. This subsample is in principle more complete because it can include objects selected with redshift-based distances $40 < d < 50$ Mpc but non-redshift distances < 40 Mpc. The slopes for M_{HI} and M_{star} are 0.16 ± 0.29 and 1.60 ± 0.29 , respectively, similar to fitting the full final sample. Directly fitting L_X as a function of both distance and M_{star} gives slopes of 0.02 ± 0.01 and 1.62 ± 0.28 ; there is no significant direct

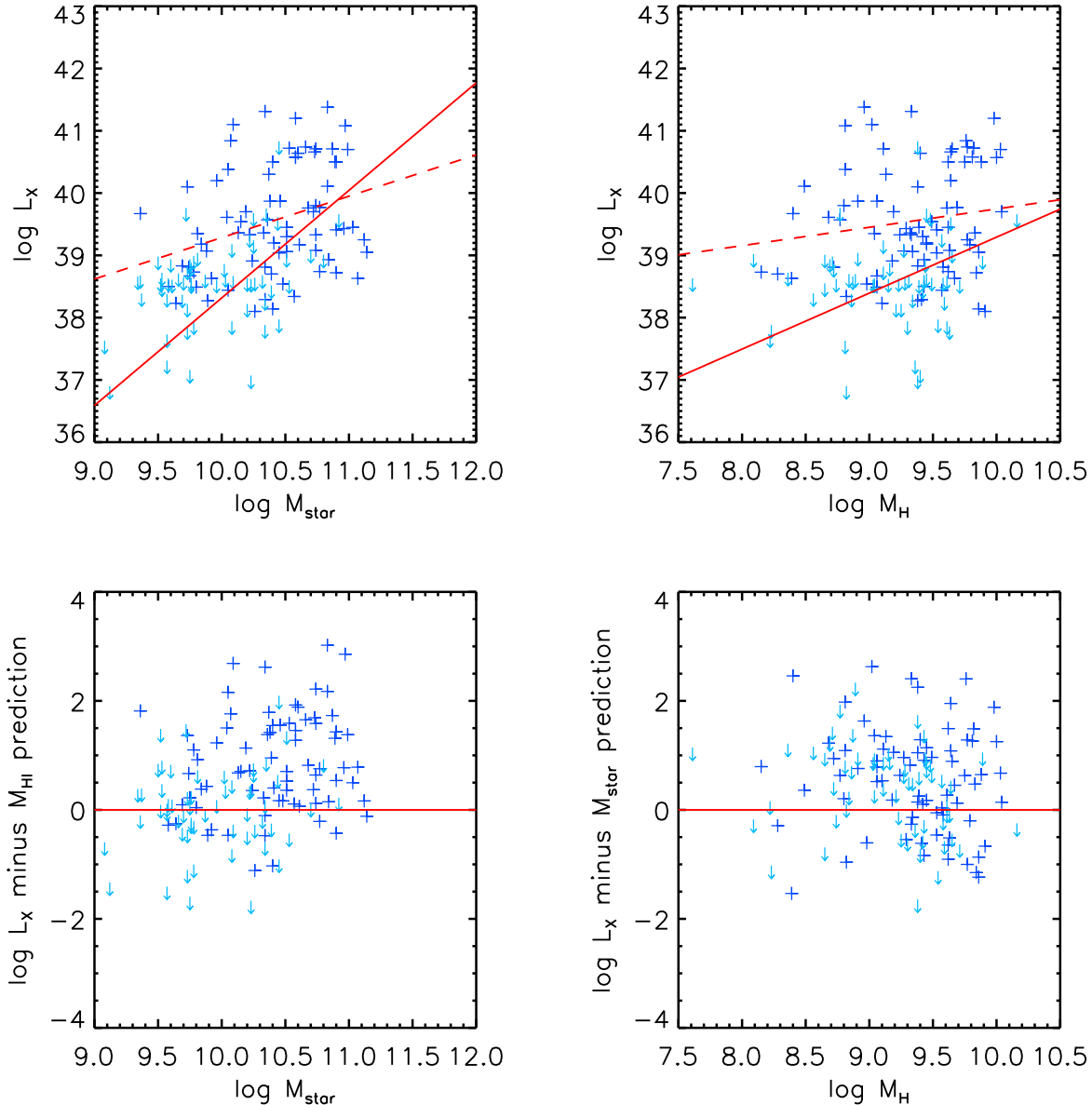


Figure 6. Top: X-ray luminosity versus stellar mass (left) and versus HI mass (right). The dashed lines are fits to detections only (plus symbols), while the solid lines are fits including the X-ray upper limits (down arrows). Measurement uncertainties of 0.2 dex and 0.1 dex were assumed for L_X and both M_{star} and M_{HI} , respectively. Linear regression was performed using the Bayesian methodology of Kelly (2007). Bottom: Residuals after subtracting the best-fit relations from the top panels. For reference, zero is marked with a solid horizontal red line.

dependence upon distance.

Finally, we used non-parametric methods to test for correlations as a complementary check to our regression analysis. Kendall’s tau values, computed within ASURV, confirm the $L_X(M_{\text{star}})$ correlation at $p < 0.0001$ and the $L_X(M_{\text{HI}})$ correlation at $p < 0.01$. We also used the Kendall’s partial tau test developed by Akritas and Siebert to test for the influence of the third variable on the L_X correlations, finding that zero partial correlation is rejected for $L_X(M_{\text{star}})$ but not for $L_X(M_{\text{HI}})$, using $p = 0.05$ here as the dividing level. These results are all consistent with the previous analysis and discussion.

3.2. X-ray binary contamination

An important caveat is that it is difficult to eliminate the chance of high-mass X-ray binary contamination in late-type galaxies, even with the outstanding angular resolution of *Chandra* (but see, e.g., Jenkins et al. 2011). The X-ray surface brightness profiles, and the independent classification of Liu (2011), suggest that at least our most luminous sources are indeed dominated by emission produced by the SMBH. Here, we estimate potential X-ray binary contamination within the *Chandra* aperture for each nuclear detection.

Low-mass X-ray binaries (LMXBs) have a luminosity

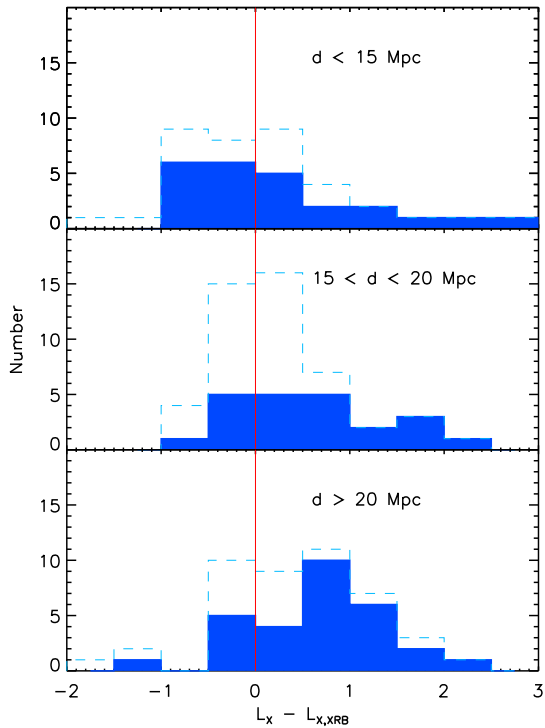


Figure 7. Difference between measured nuclear X-ray luminosities L_X and the estimated X-ray binary contamination $L_{X,XRB}$ (including both from LMXBs and HMXBs) for detected sources (filled dark blue histogram) and including limits (dashed light blue), shown for three different bins of distance. Approximately 51/75 nuclear detections are likely associated with SMBH activity.

function that scales with stellar mass (Gilfanov 2004), whereas high-mass X-ray binaries (HMXBs) have a luminosity function that scales with star formation rate (Grimm et al. 2003). This is because LMXBs are fed by Roche-lobe overflow from their low-mass long-lived companion star whereas HMXBs also accrete from the winds of their high-mass short-lived companion star. A simplified empirical recipe is given by Lehmer et al. (2008, 2010), who parameterize the total X-ray luminosity in binaries as a function of both M_{star} and SFR. They find

$$L_{X,XRB} = 9.05 \times 10^{28} M_{\text{star}} + 1.62 \times 10^{39} \text{SFR},$$

with M_{star} and SFR in units of M_{\odot} and M_{\odot}/yr , respectively. Note that this is for the hard 2–10 keV band; to convert to the full 0.5–7 keV band over which the CSC fluxes for our sources are measured, we add 0.11 dex to $L_{X,XRB}$ (determined using PIMMS for a power-law spectrum with $\Gamma=1.7$ for a typical column density of $N_{\text{H,gal}} = 2 \times 10^{20} \text{cm}^{-2}$).

We conservatively calculate $L_{X,XRB}$ within a $2''$ aperture centered on the galaxy, since the matching radius for nuclear *Chandra* sources is $2''$. We assume that the star formation throughout the galaxy follows the total light; this is also conservative as these late-type galaxies tend to have bulges redder than the disks. Rather than modeling

the surface brightness profile for each individual galaxy, we use a template to determine what fraction of the total M_{star} and SFR (and hence what fraction of the $L_{X,XRB}$) is contained within $2''$ as a function of distance. The galaxy we select as a template is NGC 3344 which has $\log M_{\text{star}} = 10.1$, $\log \text{SFR} = 0.04$, $M_B = -19.7$ (all near the median values of our final sample), and is nearby at $d \simeq 10$ Mpc. We extract the optical surface brightness within circular radial apertures (avoiding foreground stars) and model the disk plus bulge as separate Sersic profile components (Ciotti & Bertin 1999) with $n = 1$ and $n = 4$, respectively. The scaling factor for $L_{X,XRB}$ based on this template changes smoothly from 13% to 61% at distances from 5 to 50 Mpc; it may be parameterized as $0.06917 + 0.01331 \times d - 0.00005 \times d^2$ with d in Mpc. A galaxy-by-galaxy approach would provide some increase in accuracy but using a template to calculate the fractional scaling suffices for our statistical investigation. A histogram of expected values of $L_{X,XRB}$ within $2''$ is provided in Figure 7, along with the measured nuclear X-ray luminosities for our galaxies.

We then estimate the probability that the nuclear X-ray emission is associated with a SMBH rather than LMXBs or HMXBs for all sources with a nuclear X-ray source detected by *Chandra*. This is calculated as the likelihood that a random variable from a Gaussian distribution in $\log L_X$ with a mean of the scaled $\log L_{X,XRB}$ and a sigma of 0.3 dex (i.e., scatter of 2) is less than or equal to the measured nuclear $\log L_X$ for that galaxy. Those values are given in Table 1. Because most of the nuclear X-ray luminosities are greater than those typically reached by LMXBs or even HMXBs, and because the *Chandra* PSF out to our adopted distance limit only encloses the central region of each galaxy, most X-ray detections are secure. In particular, 51/75 detections have $L_X > L_{X,XRB}$ and probability > 0.5 . Revisiting the correlations of L_X with M_{HI} only, M_{star} only, and both fit jointly, the slopes when treating galaxies with probabilities < 0.5 as limits rather than detections are similar but with larger uncertainties: 0.65 ± 0.42 , 1.74 ± 0.40 , and -0.01 ± 0.40 versus 1.80 ± 0.47 , respectively.

To incorporate quantitatively the possibility of LMXB and HMXB contamination in our correlation analysis, we fit the sample 20 different times and probabilistically vary whether each X-ray source is treated as a detection or a limit. For example, a nuclear X-ray source with $L_X = 39.5$ and a probability that this is due to the SMBH rather than LMXBs or HMXBs of 0.7 is treated as a detection in 70% of the fits and as a limit in the remaining 30%. The results of these 20 fits are shown in Figure 8 for the fit of L_X as a joint function of both M_{HI} and M_{star} . In all cases, the slopes show a significant dependence on M_{star} and not on M_{HI} , and the preferred values are also within the uncertainties from the previous fit treating all detections as uncontaminated. We conclude that our results are robust against typical LMXB and HMXB binary contamination.

3.3. Other potential dependencies

In Figure 9, top left panel, we show the relationship between residual nuclear X-ray luminosity (i.e., after removing the dependence on stellar mass, so $L_X - L_X(M_{\text{star}})$) as a function of galaxy size. Galaxy size is calculated from the apparent diameter corrected for

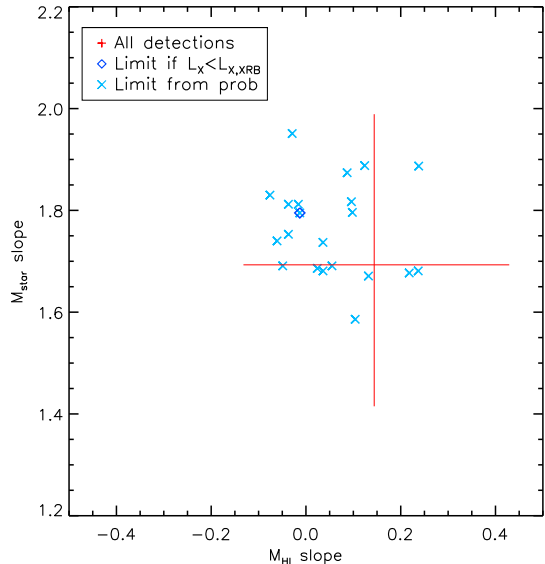


Figure 8. Slopes from the joint fit for $L_X(M_{\text{HI}}, M_{\text{star}})$ for all detections (large red cross, showing uncertainties on the parameters) and then treating only galaxies with $L_X > L_{X,\text{XRB}}$ as detections (dark blue diamond), and then 20 random trials treating detections probabilistically (light blue x marks).

galactic extinction and inclination effects, as taken from the HyperLeda database, and converted to physical size for the distances given in Table 1. Presuming a uniform surface brightness profile for our spiral galaxies (clearly incorrect but acceptable to first order for the scaling arguments considered here), galaxy size is a multiplicative constant times the effective radius. There appears to be a possible tendency for more compact galaxies to be relatively more X-ray luminous, but when we quantified this trend by fitting a linear regression model using the `linmix_err.pro` IDL routine we found that the slope was not significantly different from zero. It would be interesting to revisit this point with a larger sample. We also tested for a potential relationship between the central velocity dispersion (again from HyperLeda) and residual nuclear X-ray luminosity, as shown in the top central panel of Figure 9, and here too we do not find any significant correlation. Finally, we consider the size multiplied by the square of the velocity dispersion as a proxy for the virial mass, as shown in the top right panel of Figure 9; here too we do not find any significant correlation. We note that L_X might still scale with any of these variables separately but if they in turn scale with M_{star} then removing that dependence leaves no trend. Finally, in the bottom panels of Figure 9, we again plot residual nuclear X-ray luminosity against the galaxy size, central stellar velocity, and virial mass proxy, but now correct these too for their dependence on stellar mass. There is a possible tendency for galaxies that have larger residual central stellar velocity dispersions or virial masses, at a given stellar mass, to also have relatively larger residual nuclear X-ray luminosities. SMBHs in local galaxies correlate mostly with stellar velocity dispersion rather than stellar mass (Shankar et al. 2016), and larger values of central stellar velocity dispersion may indicate larger SMBHs (at a given stellar mass) and hence greater X-ray

luminosity at a given Eddington ratio.

4. DISCUSSION AND CONCLUSIONS

4.1. Eddington efficiencies

We investigate the SMBH duty cycles for low and high M_{star} bins, through measuring the fraction of galaxies with L_X greater than 40 in a particular M_{star} range. We calculate the fraction of galaxies with $L_X > 40$ in the 9.3 – 10.3 M_{star} bin to be $5/67 = 7.5\%$ and the fraction of galaxies with $L_X > 40$ in the 10.3 – 11.3 M_{star} bin to be $18/62 = 29\%$. The fraction of galaxies with $L_X > 40$ within the entire sample is $23/129 = 17.8\%$. This is robust to potential XRB contamination because the probabilities that the nuclear X-ray emission is associated with a SMBH are $\simeq 1$ for our galaxies with $L_X > 40$.

For our sample of late-type galaxies, we use the M-sigma relationship given in Gültekin et al. (2009) to calculate black hole masses and compare to M_{star} : $\log(M_{\text{bh}}/M_{\text{solar}}) = 8.12 + 4.24 \log \sigma / 200 \text{ km/s}$. We find on average $M_{\text{bh}} = M_{\text{star}} - 3.22$ and use this to estimate black hole mass for our sources without measured sigma. The bins of 9.3–10.3 M_{star} and 10.3–11.3 M_{star} then correspond to bins of 6.1–7.1 M_{BH} and 7.1–8.1 M_{BH} . For comparison, Goulding et al. (2010) use mid-IR selection techniques to calculate an AGN fraction of about 20% in their sample of nearby galaxies with black hole masses similar to ours; see their Figure 5. This is in rough agreement with our X-ray estimate of the fraction of SMBHs accreting at $L_X > 40$.

The late-type galaxies studied here have detected nuclear X-ray luminosities ranging from $38.1 < \log L_X < 41.4$. For a typical SMBH of a few million solar masses, achieving $\log L_X \sim 40$ with a radiative efficiency of $\epsilon \sim 0.1$ only requires $\sim 2 \times 10^{-6} M_{\odot} \text{ yr}^{-1}$. These include Seyfert AGNs as well as formally inactive galaxies; our sample probes SMBHs across a continuum of low-level accretion rates.

4.2. Multiwavelength activity indicators

We were able to use indicators at a number of wavelengths to distinguish SMBH activity from other potential sources of X-ray emission. X-ray, optical and radio emissions can be used to probe this. First, several galaxies are known Seyferts or LINERS or have variable X-ray emission, which again improves the chances that we are probing SMBH-linked activity rather than high-mass X-ray binary contamination. Seyferts have strong optical features of AGN activity that include strong emission lines as well as absorption lines from the host galaxy. Seyferts 1 and 2 are thought to be the same objects seen from different vantage points. Seyfert 1s have broadened emission lines while Seyfert 2s do not because of our viewing angle. LINERS have spectral features that could result from either low-level AGN activity or star formation.

Table 1 shows optical indicators of black hole activity for selected sources under the activity column. Several galaxies, including a high fraction of the Seyferts, also have a central continuum 1.4 GHz point source VLA detection (Ho & Ulvestad 2001; also VLA FIRST survey data; Becker et al. 1995). Radio detections serve as a signpost of SMBH activity because, in the fundamental plane (e.g., Merloni et al. 2003), the radio luminosity

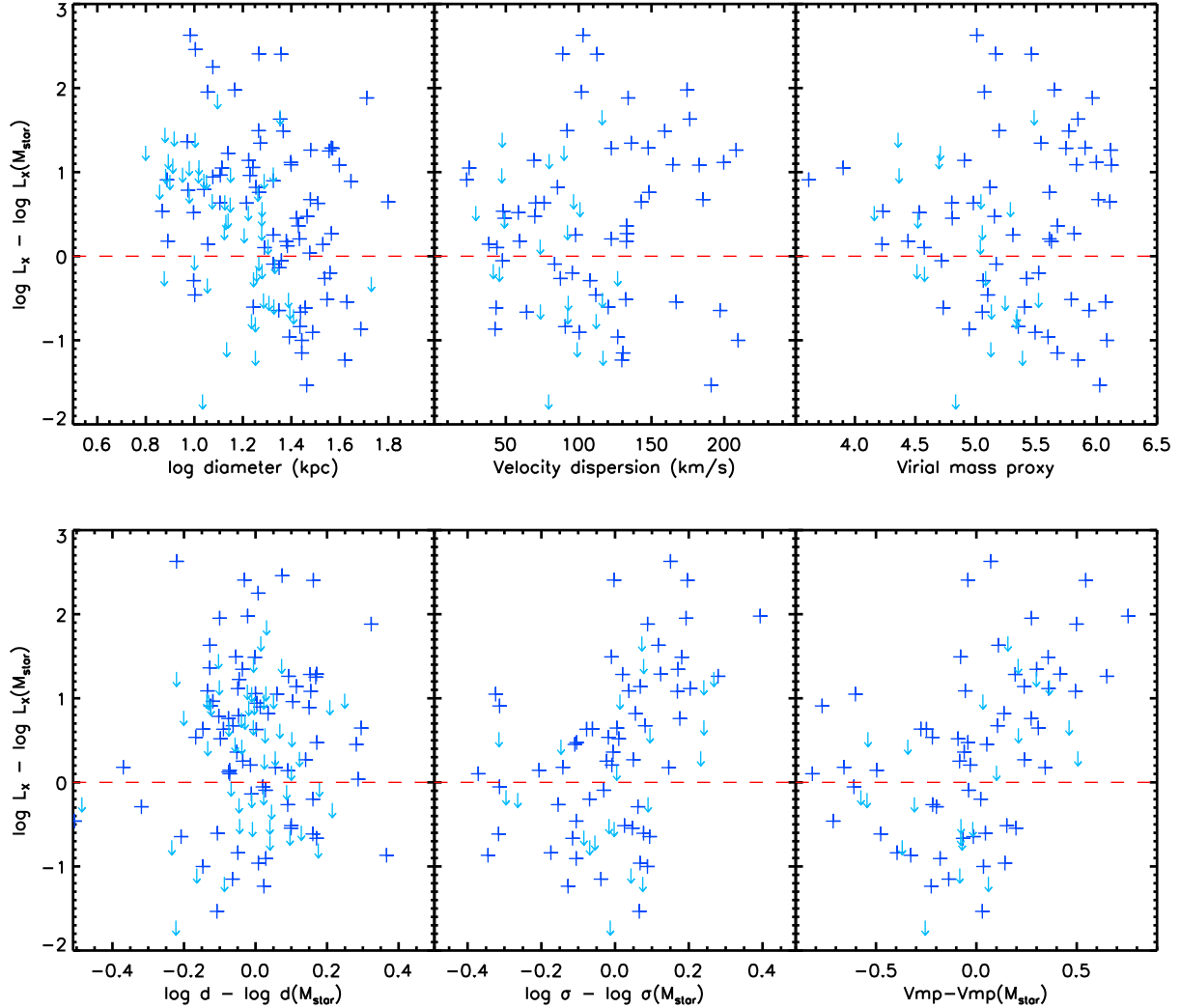


Figure 9. Top: Residual nuclear X-ray luminosity (after removing dependence on M_{star}) versus galaxy size (left), central stellar velocity dispersion (center), and a virial mass proxy (right). For reference, the dashed red line shows zero residual X-ray luminosity. There are no significant correlations present. Bottom: As above, but here the galaxy size, central stellar velocity, and virial mass proxy are also corrected for their dependence on stellar mass.

one expects is a function of the X-ray luminosity and the SMBH mass. While X-ray binaries have radio emission, at a given X-ray luminosity, a 10 solar mass XRB will have a much weaker radio luminosity than a million solar mass SMBH. Star formation processes and supernovae remnants can also produce radio sources, albeit spread throughout the external galaxy rather than centralized (note the typical angular resolution of these VLA maps is $\sim 5''$), but even compared to HMXBs supernova remnants have short lifetimes of a few hundred thousand years when they are radio bright.

The average X-ray luminosities of the galaxies identified as Seyferts or LINERS are larger than those not classified as such in NED. The detection fraction for Seyferts and LINERS is 92% (34/37) compared to 43% for optically inactive galaxies, and 79% of those detections (27/34) have $L_X > L_{X,\text{XRB}}$. Taking X-ray limits into account using ASURV (Isobe et al. 1990), Seyferts and LINERS have a (Kaplan-Meier) mean $\log L_X = 39.83 \pm 0.16$ compared to optically inactive galaxies at

$\log L_X = 38.32 \pm 0.13$, and two-sample tests indicate probabilities of $p < 0.001$ that our samples of Seyferts and LINERS versus optically inactive galaxies have the same underlying L_X distribution. Similar results hold when normalizing L_X by M_{star} . This is consistent with the optically inactive galaxies hosting SMBHs accreting at a lower rate than in the Seyferts and LINERS.

At the same time, the gas fractions of these Seyfert and LINER galaxies are similar to (if anything perhaps slightly lower than) those of optically inactive galaxies at matched M_{star} values. We checked this by drawing a random subsample without consideration of gas fraction from the optically inactive galaxies weighted to match the M_{star} distribution of the Seyferts and LINERS (achieving good agreement in M_{star} after weighting; KS test probability $p = 0.5$). The resulting M_{star} matched subsample of non-Seyferts has a distribution of gas fractions that is consistent with the Seyferts (KS test $p = 0.3$). This also suggests that SMBH accretion rates are not dependent on galaxy-wide gas fractions alone.

4.3. SFR, cold gas, and SMBH activity

Our fits test for a relationship between black hole accretion rate and HI content. Since cold gas is available for star formation, we might expect a positive trend based on the correlation between star formation rate and AGN fraction found by Rafferty et al. (2011). On the other hand, Fabello et al. (2011, 2012) find that bulge properties and SMBH accretion rate are not linked to HI gas in blue galaxies (although they do appear to correlate in red galaxies). Specifically, the gas fraction in galaxies that host AGNs does not differ from that in a matched comparison sample of galaxies, or depend on the $O\ III/M_{BH}$ accretion indicator (Fabello et al. 2011). Our results are consistent with this finding, to the extent that X-ray luminosities provide a complementary (if not entirely overlapping) view of nuclear activity. The lack of a strong dependence of L_X upon M_{HI} in our analysis suggests that the galaxy-wide cold gas does not directly influence low-level supermassive black hole activity in these spirals.

We also investigated the relationship between the presence of bar features (barred spirals) and the HI and X-ray luminosities. A bar provides gravitational torque and is believed to funnel gas down to the central regions of the galaxy by decreasing its angular momentum (e.g., Shlosman et al. 1990), so we might expect barred galaxies to have greater nuclear L_X values at a given HI mass. We identified barred galaxies using the classification in NED, as given in Table 1. From our 132 late-type galaxies, only 8 lack bar classifications in NED; 34 have no bar (type A), 39 are conclusively barred (type B), and 51 have intermediate or weak bar (type AB). We do not find any significant difference in the average nuclear X-ray luminosities of late-type galaxies with versus without bars. Specifically, barred galaxies have a (Kaplan-Meier) mean $\log L_X = 38.60 \pm 0.25$ compared to non-barred galaxies at $\log L_X = 38.87 \pm 0.23$, and two-sample tests are consistent ($p > 0.5$) with these samples having the same underlying L_X distribution. (Weakly barred galaxies have $\log L_X = 38.76 \pm 0.16$ and are also consistent with non-barred galaxies.) This suggests that bars may not channel a significant amount of gas directly into the black hole or alternatively perhaps that there is a balance between feeding and accretion. Our results are consistent with the previous findings of Zhang et al. (2009) that barred galaxies do not have greater nuclear X-ray luminosities than non-barred galaxies; if anything, those authors find that strongly barred galaxies tend to be X-ray faint. This might also be related to the results from Masters et al. (2012) that barred galaxies are generally less gas-rich, perhaps because the bar concentrates gas in the galactic center where it is rapidly consumed in star formation.

We also investigate the potential difference in X-ray luminosity between interacting and non-interacting galaxies. The nuclear X-ray detection fraction is 13/19 (68%) for galaxies flagged as “multiple” in HyperLeda, and 62/110 (56%) for the rest. The average X-ray luminosity for detected interacting/merging galaxies is 39.63 ± 0.28 and average X-ray luminosity for the non-interacting detected galaxies is 39.54 ± 0.08 . Perhaps because we do not have a large number of interacting galaxies in our sample, the difference in detection fractions and average X-ray luminosity is suggestive but not formally signifi-

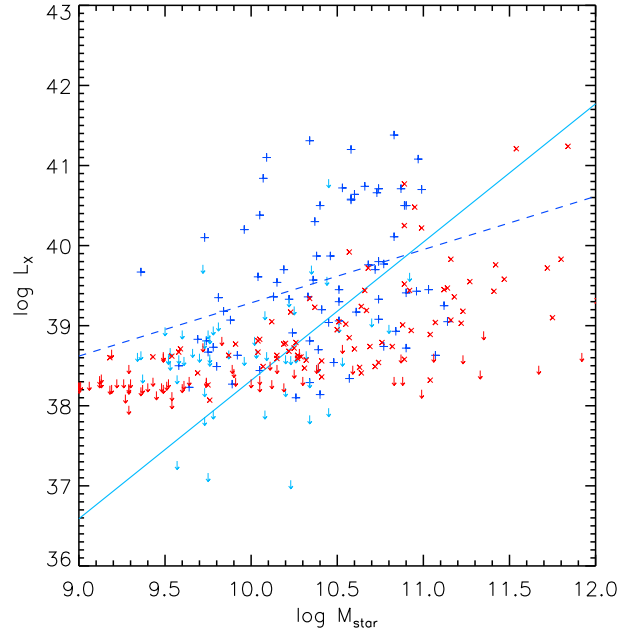


Figure 10. Nuclear X-ray luminosity as a function of galaxy stellar mass for our sample of late-type galaxies, along with the AMUSE sample of early-type galaxies. The early-type galaxies tend to have somewhat lower nuclear X-ray luminosities at a given stellar mass, and have a flatter slope when fit with a linear model.

cant. Koss et al. (2011) found that hard X-ray detected AGN at $z < 0.05$ exhibit a higher fraction of mergers.

It is interesting to compare these results to low-level SMBH activity in early-type galaxies. Ellipticals also show a trend in nuclear L_X with M_{star} (Pellegrini 2010; Gallo et al. 2010), with an apparent enhancement in scaled L_X for galaxies in sparser large-scale environments (Miller et al. 2012). A comparison of our sample of late-type galaxies to the early-type galaxies in the AMUSE project (Gallo et al. 2010; Miller et al. 2012) indicates that the ellipticals tend toward lower values of L_X at a given M_{star} (see Figure 10), and the correlation has a flatter slope. Since galaxies with a particular L_X value can have a wide range of stellar masses, it seems likely that there is a wide range in SMBH accretion rates and/or efficiencies in these weakly active systems. Because early-type galaxies in the field have more HI than their cluster counterparts (Grossi et al. 2009; Oosterloo et al. 2010), if still notably less in absolute terms than do late-type galaxies, this suggests that cold gas does play a role in nuclear activity. An analysis of dust features (from HST maps) or CO emission (from IRAM) in early-type galaxies finds that the presence of dust or CO is associated with higher Eddington ratios (i.e., $> 10^{-7}$), but that there is no correlation between the CO mass and the Eddington ratio (Hodges-Kluck et al., in preparation). This is consistent with our findings for late-type galaxies that the total amount of galaxy-wide gas on kpc scales does not directly set the SMBH accretion on pc scales, but supports the importance of cold gas as a contributing element to SMBH growth. It also aligns with Sabater et al. (2015) finding that large-scale environment and galaxy mergers are not directly responsible

for AGN activity, but central cold gas supply feeds the SMBH through secular processes, and with LaMassa et al. (2013) finding that central SFR correlates with AGN activity.

In summary, this work tests the hypothesis that more cold gas in a galaxy leads to more accretion onto the central SMBH, on average; we find that this is not supported, after accounting for the effect of galactic stellar mass. This implies that the mechanisms that directly supply SMBHs with gas near the galactic center do not know or care about the total available gas throughout the galaxy. A lack of correlation between galaxy-wide HI mass and nuclear X-ray emission suggests that the central ~ 50 pc are most relevant for SMBH feeding and that the local gas supply is only loosely linked to the outskirts. Future high angular resolution observations of the gas content and dynamics in the imminent vicinity of the SMBH, for example conducted with ALMA, could help establish a link between local cold gas and SMBH activity.

We gratefully acknowledge the UAT team for support of this work and preliminary $\alpha 70$ catalog. We also thank the NSF for partial support through grant AST-1211005. We thank the referee for helpful comments that improved this paper.

We acknowledge the usage of the HyperLeda database (<http://leda.univ-lyon1.fr>). This research has made use of the NASA/IPAC Extragalactic Database (NED) which is operated by the Jet Propulsion Laboratory, California Institute of Technology, under contract with the National Aeronautics and Space Administration. This research has made use of data obtained from the Chandra Source Catalog, provided by the Chandra X-ray Center (CXC) as part of the Chandra Data Archive.

REFERENCES

- Becker, R. H., White, R. L., & Helfand, D. J. 1995, *ApJ*, 450, 559
 Bell, E. F., & Kennicutt, R. C., Jr. 2001, *ApJ*, 548, 681
 Bell, E. F., McIntosh, D. H., Katz, N., & Weinberg, M. D. 2003, *ApJS*, 149, 289
 Bizzocchi, L., Filho, M. E., Leonardo, E., et al. 2014, *ApJ*, 782, 22
 Ciotti, L., & Bertin, G. 1999, *A&A*, 352, 447
 Davis, B. L., Berrier, J. C., Johns, L., et al. 2014, *ApJ*, 789, 124
 Evans, I. N., Primini, F. A., Glotfelty, K. J., et al. 2010, *ApJS*, 189, 37
 Isobe, T., Feigelson, E. D., Akritas, M. G., et al. 1990, *ApJ*, 364, 104
 Fabello, S., Kauffmann, G., Catinella, B., et al. 2011, *MNRAS*, 416, 1739
 Fabello, S., Kauffmann, G., Catinella, B., et al. 2012, *MNRAS*, 427, 2841
 Fitzpatrick, E. L. 1999, *PASP*, 111, 63
 Gallo, E., Treu, T., Marshall, P. J., et al. 2010, *ApJ*, 714, 25
 Gilfanov, M. 2004, *MNRAS*, 349, 146
 Giovanelli, R., Haynes, M. P., Kent, B. R., et al. 2005, *AJ*, 130, 2598
 Goulding, A. D., Alexander, D. M., Lehmer, B. D., & Mullaney, J. R. 2010, *MNRAS*, 406, 597
 Graham, A. W., & Scott, N. 2013, *ApJ*, 764, 151
 Grimm, H.-J., Gilfanov, M., & Sunyaev, R. 2003, *MNRAS*, 339, 793
 Grossi, M., di Serego Alighieri, S., Giovanardi, C., et al. 2009, *A&A*, 498, 407
 Gültekin, K., Richstone, D. O., Gebhardt, K., et al. 2009, *ApJ*, 698, 198
 Huang, S., Haynes, M. P., Giovanelli, R., & Brinchmann, J. 2012, *ApJ*, 756, 113
 Huang, S., Haynes, M. P., Giovanelli, R., et al. 2014, *ApJ*, 793, 40
 Haynes, M. P., Giovanelli, R., Martin, A. M., et al. 2011, *AJ*, 142, 170
 Ho, L. C., & Ulvestad, J. S. 2001, *ApJS*, 133, 77
 Hopkins, P. F., Cox, T. J., Younger, J. D., & Hernquist, L. 2009, *ApJ*, 691, 1168
 Jenkins, L. P., Brandt, W. N., Colbert, E. J. M., et al. 2011, *ApJ*, 734, 33
 Karachentsev, I. D., & Kaisina, E. I. 2013, *AJ*, 146, 46
 Kelly, B. C. 2007, *ApJ*, 665, 1489
 Kormendy, J., Bender, R., & Cornell, M. E. 2011, *Nature*, 469, 374
 Kormendy, J., & Ho, L. C. 2013, *ARA&A*, 51, 511
 Koss, M., Mushotzky, R., Veilleux, S., et al. 2011, *ApJ*, 739, 57
 Läscher, R., Ferrarese, L., van de Ven, G., & Shankar, F. 2014, *ApJ*, 780, 70
 LaMassa, S. M., Heckman, T. M., Ptak, A., & Urry, C. M. 2013, *ApJ*, 765, L33
 Lee, J. C., Gil de Paz, A., Tremonti, C., et al. 2009, *ApJ*, 706, 599
 Lehmer, B. D., Brandt, W. N., Alexander, D. M., et al. 2008, *ApJ*, 681, 1163
 Lehmer, B. D., Alexander, D. M., Bauer, F. E., et al. 2010, *ApJ*, 724, 559
 Liu, J. 2011, *ApJS*, 192, 10
 Maddox, N., Hess, K. M., Obreschkow, D., Jarvis, M. J., & Blyth, S.-L. 2015, *MNRAS*, 447, 1610
 Makarov, D., Prugniel, P., Terekhova, N., Courtois, H., & Vauglin, I. 2014, *A&A*, 570, AA13
 Masters, K. L., Nichol, R. C., Haynes, M. P., et al. 2012, *MNRAS*, 424, 2180
 Mathur, S., Ghosh, H., Fiore, F., & Ferrarese, L. 2010, *X-ray Astronomy 2009; Present Status, Multi-Wavelength Approach and Future Perspectives*, 1248, 241
 McConnell, N. J., & Ma, C.-P. 2013, *ApJ*, 764, 184
 McQuinn, K. B. W., Skillman, E. D., Dolphin, A. E., & Mitchell, N. P. 2015, *arXiv:1505.00791*
 Merloni, A., Heinz, S., & di Matteo, T. 2003, *MNRAS*, 345, 1057
 Miller, B., Gallo, E., Treu, T., & Woo, J.-H. 2012, *ApJ*, 747, 57
 Oosterloo, T., Morganti, R., Crocker, A., et al. 2010, *MNRAS*, 409, 500
 O’Sullivan, E., Zezas, A., Vrtilik, J. M., et al. 2014, *ApJ*, 793, 73
 Peeples, M. S., & Shankar, F. 2011, *MNRAS*, 417, 2962
 Pellegrini, S. 2010, *ApJ*, 717, 640
 Rafferty, D. A., Brandt, W. N., Alexander, D. M., et al. 2011, *ApJ*, 742, 3
 Reines, A. E., Sivakoff, G. R., Johnson, K. E., & Brogan, C. L. 2011, *Nature*, 470, 66
 Sabater, J., Best, P. N., & Heckman, T. M. 2015, *MNRAS*, 447, 110
 Salim, S., Rich, R. M., Charlot, S., et al. 2007, *ApJS*, 173, 267
 Satyapal, S., Secrest, N. J., McAlpine, W., et al. 2014, *ApJ*, 784, 113
 Shankar, F., Bernardi, M., Sheth, R. K., et al. 2016, *MNRAS*, 457, 57
 Shlosman, I., Begelman, M. C., & Frank, J. 1990, *Nature*, 345, 679
 Simmons, B. D., Lintott, C., Schawinski, K., et al. 2013, *MNRAS*, 429, 2199
 Tully, R. B., Rizzi, L., Shaya, E. J., et al. 2009, *AJ*, 138, 323
 Tzanavaris, P., Gallagher, S. C., Hornschemeier, A. E., et al. 2014, *ApJS*, 212, 9
 Zhang, W. M., Soria, R., Zhang, S. N., Swartz, D. A., & Liu, J. F. 2009, *ApJ*, 699, 281

Table 1
Sample Properties

Name	RA (deg)	Dec (deg)	Dist (Mpc)	M_B	M_{HI} (M_\odot)	M_{star} (M_\odot)	L_X (erg/s)	Prob	Bar	Mult	Act
NGC0255	11.947050	-11.468730	18.0	-19.1	9.4	9.7	<38.7		AB		
NGC0470	19.936800	3.409870	26.9	-20.1	9.4	10.4	<40.8		A	M1	F
NGC0628	24.174000	15.783320	9.0	-20.4	9.9	10.3	38.1	0.04	A		

Table 1 — *Continued*

Name	RA (deg)	Dec (deg)	Dist (Mpc)	M_B	M_{HI} (M_\odot)	M_{star} (M_\odot)	L_X (erg/s)	Prob	Bar	Mult	Act
NGC0685	26.928300	-52.761790	16.0	-19.4	9.4	9.8	<38.6		AB		
UGC01378	29.080050	73.282780	46.3	-21.7	10.2	10.9	<39.7		B		
NGC0925	36.820350	33.579000	9.2	-20.0	9.6	10.1	38.4	0.49	AB		
NGC0949	37.702950	37.136590	11.3	-18.6	8.7	9.5	<38.5		A		
NGC0988	38.866050	-9.356420	17.3	-21.0	9.2	10.2	<38.6		B		
NGC0991	38.885850	-7.155020	17.3	-18.4	9.0	9.6	<38.6		AB		
IC0239	39.115950	38.969030	10.0	-18.5	9.2	9.7	<38.2		AB		
NGC1055	40.437300	0.443180	12.3	-19.6	9.6	10.3	<38.3		B		F
NGC1068	40.669650	-0.013240	12.3	-20.9	9.0	10.8	41.4	1.00	A		Sy, F
NGC1058	40.875450	37.341100	9.9	-18.7	9.1	9.6	38.2	0.26	A		Sy
NGC1073	40.918800	1.375700	12.3	-19.3	9.4	9.7	38.8	0.98	B		
NGC1097	41.579550	-30.274970	14.2	-21.1	9.7	10.9	40.7	1.00	B		L
NGC1341	51.993300	-37.150060	19.0	-18.7	8.4	9.5	<38.7		AB		
NGC1365	53.401650	-36.140510	18.0	-21.4	9.9	10.9	40.5	1.00	B		Sy
NGC1367	53.755350	-24.933230	22.7	-20.5	9.8	10.9	40.5	1.00	AB		
NGC1493	59.364450	-46.210900	16.8	-19.4	9.3	9.9	39.1	0.98	B		
NGC1637	70.367400	-2.858090	9.8	-18.7	9.1	9.8	38.7	0.93	AB		
NGC1640	70.560600	-20.434740	16.8	-18.9	8.7	10.0	39.6	1.00	B		
NGC1703	73.217250	-59.742190	11.9	-18.6	8.9	9.6	<38.4		B		
IC0396	74.495700	68.323520	14.0	-18.9	8.2	9.8	38.7	0.90			
NGC2082	85.462950	-64.301080	13.1	-18.2	8.6	9.4	<38.4		B		
NGC2139	90.283350	-23.672410	21.0	-20.0	9.6	9.8	<37.9		AB		
NGC2276	111.804450	85.751390	30.3	-21.1	9.6	10.3	38.8	0.19	AB	M1	
NGC2500	120.471600	50.737230	15.0	-18.9	9.1	9.7	<38.8		B		
NGC2541	123.667200	49.061580	11.2	-18.7	9.4	9.4	<38.7		A		
NGC2782	138.521100	40.113770	42.1	-21.0	9.6	10.7	40.7	1.00	AB		Sy, F
NGC2841	140.510250	50.976830	14.1	-21.2	9.8	11.1	39.2	0.13	A		L, F
NGC2906	143.026050	8.441590	33.6	-20.1	9.1	10.2	<39.2				
NGC2993	146.451300	-14.368380	29.0	-19.6	9.4	9.7	40.1	1.00		M2	
NGC3066	150.545400	72.125250	28.0	-19.0	9.0	9.8	39.4	0.99	AB		
NGC3169	153.562050	3.466360	23.7	-21.0	10.0	11.0	40.7	1.00	A	M1	Sy, F
IC2560	154.077750	-33.563870	32.5	-20.9	10.0	10.6	40.6	1.00	B		Sy
NGC3185	154.410750	21.688320	26.4	-19.5	8.8	10.4	39.6	0.96	B		Sy, F
NGC3184	154.570800	41.424360	13.0	-20.2	9.4	10.3	38.3	0.04	AB		
NGC3256	156.963750	-43.903760	35.2	-21.4	9.8	10.7	40.7	1.00		M3	
NGC3314A	159.303450	-27.683760	50.6	-20.0	9.5	10.2	<39.7				
NGC3310	159.689850	53.501740	20.0	-20.4	9.6	10.0	40.2	1.00	AB		
NGC3344	160.879650	24.922150	10.0	-19.7	9.6	10.1	<38.7		AB		F
NGC3368	161.690400	11.819810	7.2	-19.6	9.0	10.5	38.5	0.21	AB		F
NGC3389	162.116400	12.533130	21.4	-19.9	9.4	9.8	39.2	0.98	A		
NGC3395	162.458850	32.982830	25.7	-20.2	9.5	9.8	<38.6		AB	M2	
NGC3507	165.855750	18.135990	20.9	-19.7	9.3	10.1	39.4	0.98	B		F
NGC3521	166.452450	-0.035780	11.2	-21.0	9.8	10.9	38.7	0.03	AB		
NGC3568	167.702400	-37.447790	40.4	-21.2	10.0	10.7	39.7	0.73	B		
NGC3556	167.878950	55.674150	9.6	-19.9	9.4	10.2	<37.1		B		
NGC3627	170.062500	12.990990	8.3	-20.5	8.8	10.6	38.3	0.03	AB	M0	L, F
NGC3631	170.262000	53.169940	18.0	-20.8	9.4	10.5	39.3	0.78	A		
NGC3683	171.882600	56.876990	25.9	-19.8	9.5	10.2	39.5	0.96	B		
NGC3718	173.145150	53.067870	17.1	-20.0	9.8	10.5	40.7	1.00	B	M1	L, F
NGC3887	176.769150	-16.854710	18.2	-20.2	9.4	10.3	<38.7		B		
NGC3898	177.313650	56.084030	22.1	-20.8	9.6	11.0	39.5	0.27	A		F
NGC3913	177.662250	55.353900	17.1	-18.0	8.9	9.3	<38.7		A		
NGC3938	178.205700	44.120800	17.1	-20.4	9.6	10.3	<38.6		A		
NGC3982	179.117250	55.124930	20.5	-19.9	9.2	10.2	39.3	0.95	AB		Sy, F
UGC06930	179.323050	49.283720	17.1	-18.6	9.3	9.7	<38.6		AB		
NGC4020	179.736150	30.412470	14.3	-18.2	8.7	9.5	<39.0		B		
NGC4102	181.597800	52.710970	17.1	-19.5	8.8	10.1	40.4	1.00	AB		L, F
NGC4136	182.323800	29.927670	16.3	-19.1	9.4	9.9	38.3	0.24	AB		
NGC4151	182.635950	39.405790	11.2	-19.2	9.0	10.1	41.1	1.00	AB		Sy, F
NGC4254	184.706550	14.416410	16.8	-20.9	9.7	10.5	<38.6		A		
NGC4258	184.740000	47.303880	7.6	-20.9	9.6	10.7	39.8	0.99	AB		Sy, F
NGC4274	184.960650	29.614290	16.3	-20.2	8.7	10.8	<39.0		B		L, F
NGC4303	185.478900	4.474180	17.6	-21.2	9.8	10.6	39.2	0.53	AB		Sy, F
NGC4321	185.728200	15.821890	15.2	-21.1	9.4	10.8	38.9	0.04	AB		
NGC4414	186.612600	31.223390	17.7	-20.8	9.5	10.9	39.4	0.46	A		
NGC4411A	186.625050	8.871670	16.8	-18.1	9.0	9.6	<38.6		B		
NGC4411B	186.696750	8.884500	16.8	-18.3	9.2	9.5	<38.6		AB		
NGC4355	186.727650	-0.877560	29.0	-18.8	8.7	9.7	38.8	0.81	AB		Sy
NGC4448	187.064400	28.620310	16.3	-19.4	8.1	10.5	<39.0		B		
NGC4450	187.123350	17.084990	16.8	-20.6	8.5	10.8	40.1	0.99	A		L, F
NGC4470	187.407450	7.823900	16.8	-18.4	8.7	9.6	<38.9		A		
NGC4492	187.748850	8.077690	16.8	-18.1	7.6	9.5	<38.6		A		
NGC4498	187.914900	16.852790	16.8	-18.9	8.9	9.8	<39.0		AB		
NGC4501	187.996950	14.420140	16.8	-21.6	9.3	11.0	39.4	0.43	A		Sy, F
NGC4548	188.860200	14.496010	16.2	-20.4	8.8	10.7	39.8	0.97	B		L
NGC4559	188.990400	27.959680	8.7	-20.1	9.7	9.9	38.6	0.84	AB		

Table 1 — *Continued*

Name	RA (deg)	Dec (deg)	Dist (Mpc)	M_B	M_{HI} (M_\odot)	M_{star} (M_\odot)	L_X (erg/s)	Prob	Bar	Mult	Act
NGC4579	189.431400	11.818000	16.8	-21.0	8.8	11.0	41.1	1.00	AB		Sy, F
NGC4639	190.718250	13.257040	22.0	-19.9	9.3	10.3	41.3	1.00	AB		Sy
NGC4647	190.885500	11.582210	16.8	-19.3	8.7	10.0	<38.9		AB	M1	
NGC4651	190.927650	16.393390	16.8	-20.2	9.6	10.2	<39.3		A	M0	
NGC4654	190.985850	13.126570	16.8	-20.7	9.5	10.4	39.0	0.57	AB		
NGC4666	191.286000	-0.461860	15.7	-20.3	9.3	10.5	39.1	0.55	AB		
NGC4689	191.939850	13.762720	16.8	-19.9	8.7	10.2	<38.6		A		
NGC4713	192.491100	5.311290	15.6	-18.9	9.4	9.6	38.5	0.18	AB		
NGC4750	192.530100	72.874470	26.2	-20.3	9.1	10.4	40.3	1.00	A		L
NGC4725	192.610950	25.500910	12.4	-20.8	9.6	10.7	39.1	0.37	AB		Sy
NGC4736	192.720750	41.119990	4.4	-19.7	8.3	10.4	38.7	0.64	A		Sy, F
NGC4772	193.371600	2.168330	15.6	-19.4	8.9	10.5	39.9	1.00	A		L, F
UGC08041	193.802700	0.116680	23.0	-18.8	9.4	9.8	<38.9		B		
NGC4826	194.182500	21.681950	4.4	-19.5	8.2	10.3	<37.9		A		Sy, F
NGC4900	195.163350	2.501010	15.6	-19.2	9.1	9.8	38.5	0.09	B		
NGC4904	195.244350	-0.027520	23.0	-19.6	9.3	10.1	<39.2		B		F
NGC5033	198.364650	36.593710	18.5	-21.3	10.0	10.6	41.2	1.00	A		Sy, F
NGC5055	198.955500	42.029220	9.0	-20.9	9.6	10.8	38.7	0.10	A		
NGC5068	199.728900	-21.039050	9.0	-19.7	9.3	10.1	<37.9		AB		
NGC5194	202.469550	47.195150	8.4	-21.3	9.3	10.7	39.3	0.81	A	M2	Sy, F
NGC5240	203.979900	35.588250	35.8	-19.3	9.0	10.0	<38.6		B		
NGC5347	208.324200	33.490800	39.0	-19.8	9.6	10.4	40.5	1.00	B		Sy, F
NGC5350	208.340100	40.363940	30.9	-20.6	9.7	10.8	39.8	0.82	B		F
NGC5457	210.802500	54.349060	7.0	-20.9	9.9	10.4	38.1	0.03	AB	M0	
NGC5427	210.858750	-6.030590	27.0	-20.4	9.8	10.3	39.4	0.29	A	M2	Sy, F
UGC09235	216.175650	35.267150	47.0	-18.7	8.8	9.7	<39.8		B		
NGC5656	217.606200	35.320910	48.8	-20.5	9.5	10.4	<38.0				
NGC5678	218.023350	57.921420	27.9	-20.4	9.4	10.4	39.2	0.22	AB		
NGC5643	218.169600	-44.174480	11.8	-20.4	9.1	10.4	39.9	1.00	AB		Sy
NGC5728	220.599600	-17.253010	24.8	-20.4	9.1	10.7	40.7	1.00	AB		Sy
NGC5774	223.427100	3.582530	19.8	-18.9	9.6	9.7	<37.9		AB	M1	
ESO386-039	224.105550	-37.600920	37.0	-20.3	9.4	10.3	<39.8		B	M1	
NGC5954	233.646000	15.199390	25.5	-20.0	9.2	10.2	38.9	0.49	AB	M2	
NGC5970	234.625050	12.186110	29.8	-20.8	9.7	10.7	<39.1		B		
NGC6500	268.999050	18.338290	46.3	-20.9	9.8	10.6	40.6	1.00	A	M0	F
NGC6643	274.943100	74.568390	20.6	-20.6	9.4	10.4	<38.5		A		
NGC6764	287.068200	50.933190	23.3	-19.8	9.2	10.2	39.7	1.00	B		
ESO184-060	290.672250	-54.585270	41.1	-18.8	9.2	9.8	<38.9		AB		
UGC11466	295.744800	45.298110	18.1	-18.9	9.9	9.8	<39.0				
NGC7314	338.941650	-26.050500	15.9	-20.1	9.2	10.2	<38.2		AB		Sy
NGC7320	339.014250	33.948160	12.9	-18.1	8.4	9.4	39.7	1.00	A		
NGC7331	339.267300	34.415620	14.7	-21.6	9.9	11.1	39.0	0.03	A		L
NGC7424	344.326500	-41.070640	7.9	-19.0	9.4	9.6	<37.3		AB		
NGC7552	349.044900	-42.584280	18.7	-20.3	9.4	10.5	39.5	0.89	B		
NGC7582	349.596750	-42.369990	18.7	-20.5	9.4	10.6	40.6	1.00	B		Sy
IC5325	352.180950	-41.333390	18.7	-19.7	8.8	10.0	<38.7		AB		
IC5332	353.614500	-36.101450	9.9	-18.8	9.4	9.8	<37.2		A		
NGC7714	354.058800	2.155020	35.0	-20.2	9.8	10.1	40.8	1.00	B	M2	F
NGC7716	354.131100	0.297290	35.0	-20.2	9.6	10.4	<39.6		AB		
NGC7727	354.974400	-12.292840	26.9	-20.9	8.4	11.1	38.6	0.00	AB	M3	
NGC7741	355.976850	26.075470	15.1	-19.7	9.3	9.9	<38.7		B		

Note. — HI mass, stellar mass, and X-ray luminosity are expressed as logarithms. Prob (probability) is the estimated likelihood that the detected nuclear X-ray source is associated with a SMBH rather than X-ray binary contamination. Bar has A for no bar, AB for weak or intermediate bar, and B for barred galaxies, taken from NED. Act (activity) has Sy for Seyfert 1 or 2, L for LINER, and F for FIRST radio point source (except NGC 6500 is marked F for flat spectrum radio source from NED).